

QuBridge: Layer-wise Fidelity Decomposition in Quantum Computation Pipeline

Kisho Sotokawa¹, Hideaki Kawaguchi¹, Shin Nishio^{1,2}, and Takahiko Satoh³

¹Graduate School of Science and Technology, Keio University, Yokohama, Kanagawa 223-8522, Japan

²Department of Physics & Astronomy, University College London, London, WC1E 6BT, United Kingdom

³Faculty of Science and Technology, Keio University, Yokohama, Kanagawa 223-8522, Japan

Corresponding author: Kisho Sotokawa (e-mail: kishousotokawa@keio.jp)

Abstract—Running a quantum circuit on current hardware involves a sequence of engineering decisions, each with tunable parameters and distinct error characteristics. Existing tools optimize each decision in isolation, leaving practitioners unable to determine how much each decision contributes to final output quality. We present QuBridge, a pipeline analysis tool that decomposes quantum computation into three decision layers and measures each layer’s fidelity contribution through progressive ablation and isolation experiments. Applied to quantum teleportation under IBM-calibrated noise models, the framework surfaces three phenomena that end-to-end measurement obscures. Qubit selection narrows the worst-case fidelity band from 11.8% to under 2% with downstream layers held fixed, without changing the peak. Per-gate pulse-shape assignment adds a +0.9% residual gain whose attributed magnitude depends on upstream layout. Error-detection encoding is not uniformly advantageous, and its conditional benefit emerges for input states whose dominant error channel is detectable by the chosen code. QuBridge operates on cached calibration data without requiring live hardware access.

Index Terms—quantum software engineering, fidelity decomposition, pipeline decomposition, noise-aware compilation, qubit selection, quantum teleportation, IBM Quantum

I. INTRODUCTION

Executing a quantum circuit on current hardware requires a chain of engineering decisions. The practitioner chooses which backend to target, which physical qubits to allocate, how transpilation maps logical operations to the device’s native gate set, and how to shape the control pulses that drive each gate. On noisy intermediate-scale quantum (NISQ) devices [1], each decision constrains downstream options and introduces its own error channel. However, existing work evaluates these decisions separately. Noise-aware mapping strategies [2], [3] assess layout quality without accounting for subsequent transpilation. Pulse optimization is studied independently of qubit placement [4]. When output fidelity changes, practitioners cannot determine which layer caused the gain or regression, nor whether an upstream improvement survives downstream transformations at all.

This pipeline structure marks the boundaries where theoretical equivalence breaks under physical constraints. Mathematically equivalent input states, topologically equivalent qubit placements, and unitary-equivalent gate decompositions yield different hardware outcomes through state-dependent dephasing, spatial noise heterogeneity, and spectral leakage respectively.

Current tools do not expose these boundaries. Circuit simulators such as Quirk [5] enable gate-level exploration without hardware context. Quantum compilers including Qiskit [6], tket [7], and BQSKit [8] optimize individual compilation passes but return only a final compiled circuit. Per-pass fidelity contributions are not reported. Visualization platforms such as IBM Quantum Composer [9] and Quantum Flytrap [10] address single stages in isolation. The quantum software engineering community [11], [12] has begun formalizing testing and quality-assurance methodologies [13], but no existing tool measures whether an improvement at one decision, such as selecting lower-error qubits, actually survives subsequent transpilation and noise, or is silently absorbed by later decisions.

We address this attribution problem through layer-wise fidelity decomposition, the attribution of end-to-end fidelity change to individual pipeline layers, each traceable to a dominant hardware-level error mechanism. We operationalize this through two complementary protocols. Progressive ablation optimizes one layer while randomizing the rest, measuring that layer’s contribution as a reduction in fidelity band width. Isolation experiments fix all other layers and vary a single parameter set to expose one layer’s sensitivity profile. Quantum teleportation [14] serves as the primary benchmark because it exposes layer-wise structure clearly. The same three theoretical breakpoints described above appear at distinct, identifiable points in the protocol, and its compact circuit size makes noise contributions attributable rather than conflated.

We present QuBridge, a pipeline analysis tool that decomposes quantum computation into three decision layers (state preparation, qubit selection, and pulse-shape assignment) plus a results layer, and measures each layer’s fidelity contribution. We validate on physical (three-qubit) and error-detected (six-qubit) quantum teleportation using noise-model simulation calibrated to IBM Torino (133-qubit Heron architecture).

Rather than automating pipeline optimization, QuBridge is designed as an exploratory environment where practitioners can observe how decisions at each layer, including error-detection encoding, shape end-to-end fidelity. The tool’s value lies in making improvement mechanisms visible rather than in producing optimal circuits automatically. Our contributions are threefold.

- 1) We present QuBridge, a pipeline analysis tool that decomposes quantum execution into three decision lay-

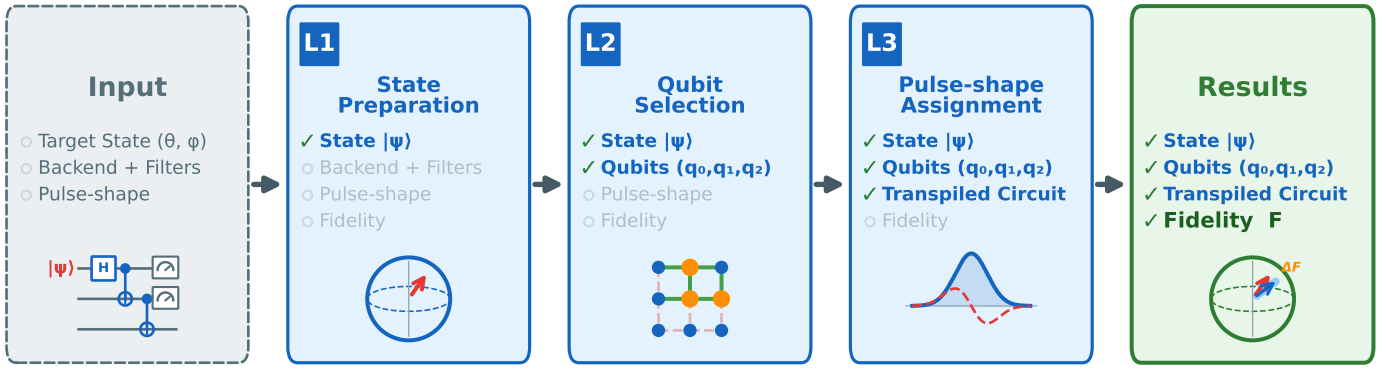


Fig. 1. QuBridge pipeline architecture. Three decision layers plus Results decompose quantum computation into separately tunable layers. Each layer progressively accumulates pipeline outputs (checked items), culminating in the final fidelity F at Results. Both physical (3-qubit) and error-detected (6-qubit) modes share this structure.

ers and reports per-layer fidelity contributions through progressive ablation and isolation experiments, operating on cached calibration data without live hardware access.

- 2) We ground layer-wise fidelity decomposition in the theory-hardware boundary, where each layer is motivated by a point where theoretically equivalent decisions yield physically distinct outcomes, making per-layer attribution operationally meaningful.
- 3) Applied to physical and error-detected teleportation, the framework surfaces three phenomena that end-to-end measurement obscures. Qubit selection acts on the worst-case rather than the peak fidelity. Per-layer contributions are context-dependent with respect to upstream state. Error-detection encoding is not uniformly advantageous, and its conditional benefit emerges for input states whose dominant error channel is detectable by the chosen code.

II. RELATED WORK

Tools for quantum execution pipelines. Quantum compilers including Qiskit [6], tket [7], and BQSKit [8] optimize individual compilation passes and return a final compiled circuit. Qiskit’s PassManager exposes per-pass callbacks for intermediate inspection, but at the granularity of compilation passes rather than decision layers that map to distinct physical error mechanisms. Noise-aware mapping strategies [2], [3] and VF2 subgraph matching [15] improve qubit layout selection but evaluate this stage in isolation. Visualization platforms such as Quirk [5], IBM Quantum Composer [9], Quantum Flytrap [10], and QuTiP Virtual Lab [16] address single stages without exposing per-layer fidelity attribution. Recent quantum software debugging tools [17] target test generation and assertion checking, and QuBridge addresses the orthogonal problem of attributing fidelity changes to pipeline decisions.

Attribution and decomposition. Attributing observed behavior to individual components is a recurring pattern in software engineering. Delta debugging [18] progressively isolates the change responsible for a regression by ablating one factor at a time, and spectrum-based fault localization [19] attributes test failures to specific code locations through similar

ablation-style reasoning. While testing and quality assurance for quantum software is being formalized [11]–[13], per-layer fidelity attribution remains unaddressed for the quantum execution pipeline. QuBridge applies the progressive-ablation pattern to the quantum execution pipeline, where each layer corresponds to a dominant hardware-level error mechanism rather than an arbitrary software boundary.

III. SYSTEM DESIGN

A. Pipeline Architecture

QuBridge decomposes quantum computation into three decision layers (L1–L3) plus Results (Fig. 1). Each decision layer exposes tunable parameters whose downstream fidelity effects are measured in Section IV. Results is a measurement stage that reports F and per-layer contributions, not a decision layer.

The system supports two teleportation modes sharing the same pipeline, **physical** (three-qubit) and **error-detected** (six-qubit with $[[2, 1, 1]]$ repetition code encoding).

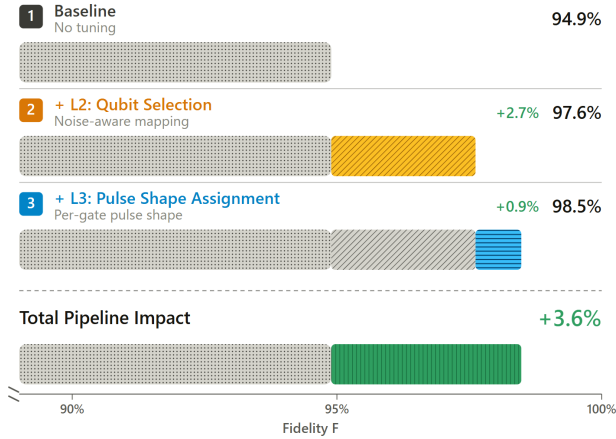
State preparation (L1). The input state $|\psi\rangle = \cos(\theta/2)|0\rangle + e^{i\phi}\sin(\theta/2)|1\rangle$ is prepared using $R_y(\theta)$ and $R_z(\phi)$ gates, parameterized via interactive Bloch sphere sliders.

Qubit selection (L2). L2 selects the physical qubits and coupling-map edges on which the circuit executes. Mode-specific mechanisms (threshold filtering, VF2 subgraph matching) are detailed in §IV-B and §IV-D.

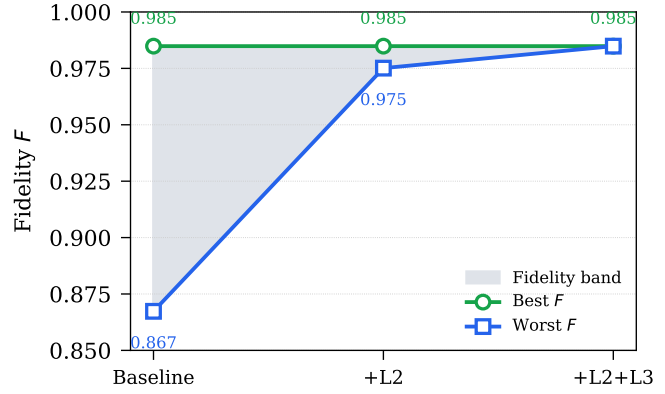
Pulse-shape assignment (L3). L3 assigns a pulse envelope (Square, Gaussian Square, or derivative removal by adiabatic gate (DRAG)) to each native gate type in the transpiled circuit. Duration and amplitude are fixed by calibration, so L3 controls only the envelope shape.

Results. In the current implementation, we visualize the preparation and output of single-qubit states via Bloch sphere rendering, suited to the teleportation workload demonstrated in this paper. The Results layer is modular, and alternative renderers such as expectation-value plots or measurement histograms can be substituted for circuits with different output structures.

To make per-layer contributions observable during interactive use, Results presents a **Layer Fidelity Waterfall** (Fig. 2a)



(a) Waterfall view.



(b) Progressive ablation result.

Fig. 2. Results and Pipeline Decomposition. (a) Illustrative rendering of the Waterfall view, which decomposes the +3.6% pipeline gain into Baseline, +L2 (Qubit Selection), and +L3 (Pulse-shape Assignment). Numbered badges (1, 2, 3) act as live Fidelity Actions buttons that add each data point. (b) Band width narrows as L2 and L3 are progressively optimized, confirming L2 provides the largest band narrowing.

that decomposes the total fidelity improvement into per-layer bars, a baseline (default qubits, no pulse-shape assignment) plus the incremental gain from each pipeline decision (L2 noise-aware qubit selection, L3 per-gate pulse-shape assignment).

This paper empirically focuses on L2, L3, and one encoding-mediated interaction case. L1 is exposed as an interactive control surface rather than systematically swept, and its quantitative contribution is not reported here.

B. Error-Detection Encoding

Encoding as a meta-decision. Encoding is a meta-decision that reshapes the L2 layout landscape rather than acting as a separate decision layer.

The error-detected mode uses a $[[2, 1, 1]]$ repetition code, with encoded states $|0_L\rangle=|00\rangle$ and $|1_L\rangle=|11\rangle$, and logical operators $X_L=X\otimes X$ and $Z_L=Z\otimes I$. This yields a six-qubit circuit (Alice qubits 0–1, Mediator 2–3, Bob 4–5) with 8 two-qubit gates, amounting to $4.0\times$ the physical circuit’s 2 two-qubit gates. The code detects single bit-flip errors by flagging measurement outcomes outside $\{00, 11\}$, enabling syndrome-based post-selection without ancilla overhead. This code is chosen because its compact circuit graph maps to many adjacent configurations on current hardware, enabling layouts that minimize routing overhead and preserve the detection margin.

IV. EVALUATION

We evaluate layer-wise fidelity decomposition through four experiments. Progressive ablation tests whether per-layer contributions can be isolated (§IV-A). An L2 isolation sweep identifies why qubit selection produces the largest band narrowing (§IV-B). An L3 isolation experiment quantifies the effect of per-gate pulse-shape assignment (§IV-C). Extension to error-detection encoding tests whether the framework generalizes (§IV-D). The primary metric is state fidelity $F = \langle \psi | \rho | \psi \rangle$,

which directly measures teleportation quality. Across the progressive ablation experiments (§IV-A, §IV-D), we quantify a layer’s *fidelity contribution* as the band narrowing it induces. We define $C_\ell = \text{Band}_{\text{before fixing } \ell} - \text{Band}_{\text{after}}$, where $\text{Band} = F_{\text{best}} - F_{\text{worst}}$ is the width of the fidelity distribution over pipeline configurations. Throughout this section, Band is operationalized as the gap from the worst surviving configuration in a given setting to the best observed pipeline configuration $F = 0.985$, which serves as a practitioner-facing fixed reference. We use band narrowing as the contribution metric because the practitioner-facing question is not only how high fidelity can be made, but how safely poor configurations can be excluded.

All fidelity values are computed via density-matrix simulation under a noise model built from cached calibration data of IBM Torino (133 qubits, Heron architecture, calibration snapshot 2026-01-16). Each gate’s error channel is constructed as a composition of thermal relaxation (T_1 , T_2) and a sparse Pauli-Lindblad residual term [20], [21], with Pauli generators weighted by decoherence fractions anchored on randomized-benchmarking rates. Readout is modeled as a calibrated asymmetric confusion matrix. Circuits are transpiled with Qiskit 1.3.1 at optimization level 3, and simulation uses Qiskit Aer 0.16.0 [22]. Density-matrix simulation is deterministic, so per-configuration repeats in the tables ensure logging-schema consistency across experiments rather than providing statistical noise estimates. Unless stated otherwise, experiments use the stress-test state $|+\rangle$, which is maximally sensitive to the dephasing channel that dominates at our circuit depth. §IV-D extends to $|1\rangle$ to expose state-dependent behavior under T_1 decay.

For interpretability, the progressive ablation baseline fixes L3 to the uniform All-Square setting while varying L2 across random configurations. We then expose the residual L3 sensitivity after fixing the best L2 path. This layered construction, rather than strict simultaneous randomization, is what Table I

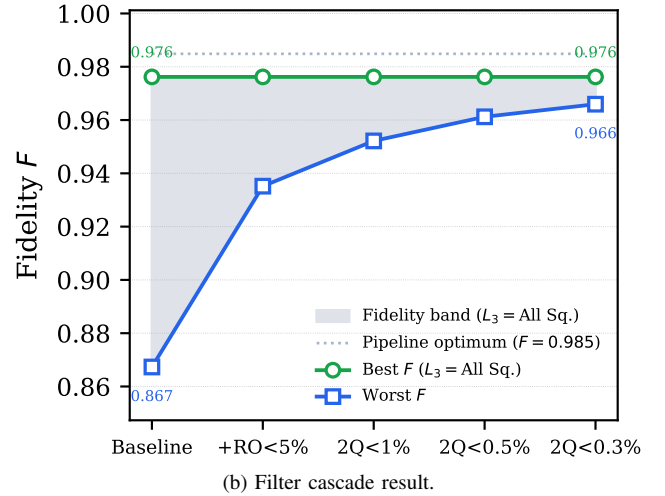
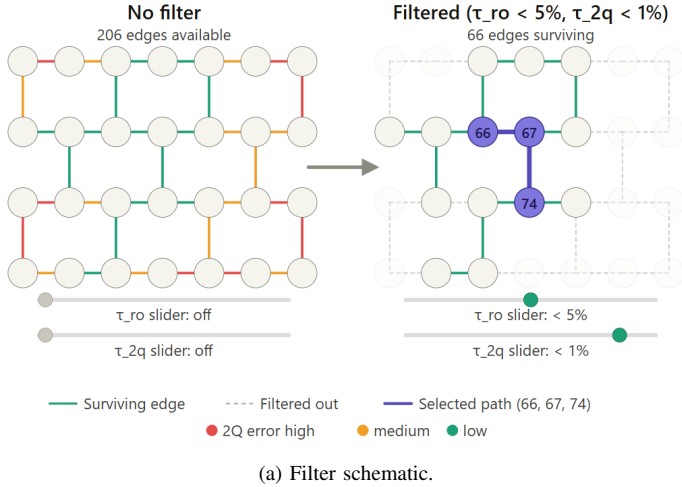


Fig. 3. L2 Qubit Selection. (a) Illustrative rendering of the filter panel. Edges are colour-coded by 2Q gate error (red high, green low). Sliders τ_{ro} and τ_{2q} progressively prune high-error edges, narrowing the edge pool from 206 to 66. The surviving subgraph (highlighted triplet (66, 67, 74)) is what the user selects from. Edge count and the corresponding number of three-qubit candidate paths through the filtered subgraph are reported separately in Table II. (b) The fidelity band narrows (11.8% \rightarrow 1.9%) across the cumulative filter cascade. Best $F=0.985$ is the pipeline optimum, reached in Fig. 4b via L3 tuning.

reports.

A. End-to-End Pipeline Trace

We first test whether each layer’s fidelity contribution can be isolated when the others are randomized, then trace how QuBridge surfaces this decomposition to a practitioner.

Diagnostic vignette. A practitioner prepares $|+\rangle$ for teleportation on IBM Torino. Starting from a topology-valid but not noise-aware qubit path and a uniform Square pulse-shape, she observes $F = 0.949$. Activating L2 with noise-aware mapping selects the surviving path (66, 67, 74) and raises fidelity to $F = 0.976$, and activating L3 with per-gate pulse-shape assignment further raises it to $F = 0.985$. The Waterfall (Fig. 2a) decomposes the cumulative +3.6% improvement into per-layer bars live.

Without QuBridge, Qiskit’s `transpile()` would have returned only the final compiled circuit; the practitioner would observe $F = 0.985$ from end-to-end measurement, with no visibility into how L2 and L3 each contributed to the +3.6% gain.

Systematic validation. To confirm that the vignette reflects a reproducible decomposition rather than a favorable path, we sweep random configurations with one layer progressively fixed (Fig. 2b, Table I). The fidelity band narrows from 11.8% (L3 fixed at All Square, L2 randomized) to 1.0% once L2 is fixed to the noise-aware path. The residual gap is then closed by L3 per-gate assignment, which deterministically selects the per-gate optimum ($F = 0.985$). Best F pins at 0.985 once L2 is fixed, confirming that L2 determines the reachable ceiling while L3 closes the residual worst-case gap. This collapse from the 11.8% baseline band is the framework’s quantitative signature. Per-layer contributions are separable, and the tool renders that separability visible at interaction time.

TABLE I
PIPELINE BAND NARROWING AS L2 AND L3 ARE PROGRESSIVELY OPTIMIZED

Layer	n	Worst F	Band
Baseline (all L2 paths, L_3 =All Sq.)	184	0.867	11.8%
+L2 (fix qubits, L_3 varies)	4	0.975	1.0%
+L2+L3 (fix qubits, L_3 =per-gate opt.)	1	0.985	0.0%

Each row sweeps the layers not yet fixed (L2 paths in row 1; L3 shapes in row 2; row 3 fixes both), where n counts the distinct configurations and each is averaged over three repeats. The fixed L2 path is (66, 67, 74). The collapse of the band to zero once both layers are fixed is the framework’s quantitative signature, with the reachable ceiling pinned at $F = 0.985$.

B. L2 Sensitivity

We fix L1 and L3 and perform an isolation sweep of L2’s filtering parameters, identifying the physical mechanism through which qubit selection controls fidelity.

Two filter sliders (readout error τ_{ro} and 2Q gate error τ_{2q}) progressively prune high-error edges from the coupling map (Fig. 3a), yielding a filtered subgraph G_τ . Filtering does not change the best achievable fidelity but raises the worst-case by excluding low-quality paths. We apply filters cumulatively and measure fidelity on the best and worst surviving paths ($n=60$, two input states, three repeats).

As shown in Table II and Fig. 3b, the readout error threshold τ_{ro} provides the largest single improvement (F_{worst} goes from 0.867 to 0.935), and subsequent tightening of the 2Q gate threshold τ_{2q} closes the remaining gap. At the strictest filtering, the fidelity band collapses to 1.9%, and any surviving path achieves near-optimal fidelity.

C. L3 Sensitivity

We fix L1 and L2 and vary L3’s pulse-shape assignment in isolation.

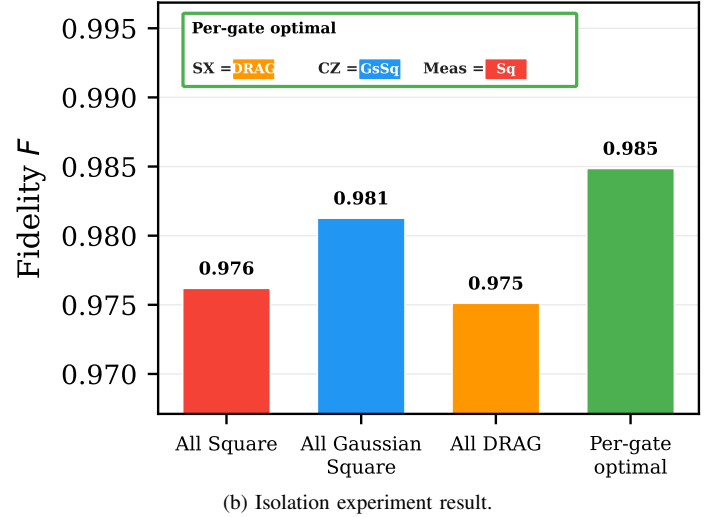
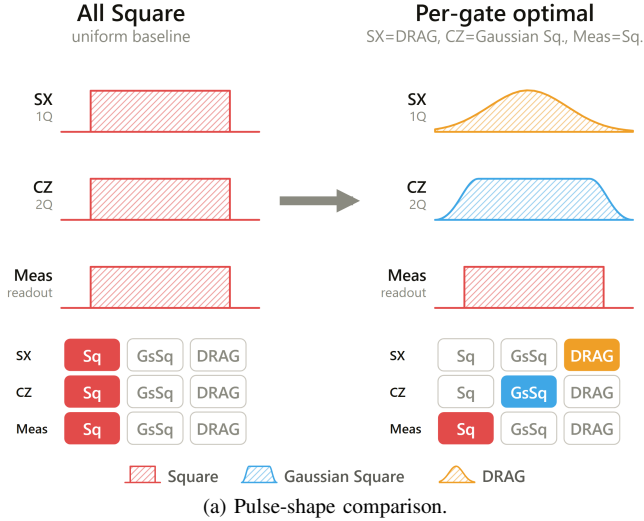


Fig. 4. L3 Pulse-shape Assignment. (a) Illustrative rendering of the pulse-shape selector. The left panel shows the uniform All Square baseline (red hatched pulses for SX, CZ, Meas), and the right panel shows per-gate optimal (SX=DRAG orange, CZ=Gaussian Square blue, Meas=Square red). The 3×3 selector matrix lets users pick a shape per gate type, with the coloured cell indicating the active choice. (b) Per-gate optimal outperforms every uniform shape, achieving $F=98.49\%$, $+0.87\%$ over the All Square baseline (Fig. 3b endpoint).

TABLE II
CUMULATIVE L2 FILTERING ON IBM TORINO

Filter	Paths	Worst F	Band
Baseline	184	0.867	11.8%
$+\tau_{ro} < 5\%$	67	0.935	5.0%
$+\tau_{2q} < 1\%$	63	0.952	3.3%
$+\tau_{2q} < 0.5\%$	48	0.961	2.4%
$+\tau_{2q} < 0.3\%$	27	0.966	1.9%

The “Paths” column counts the three-qubit candidate paths admitted by the cumulative threshold filter; the underlying coupling-graph edge count is shown in Fig. 3a. The baseline filter requires $T_1 \geq 30 \mu\text{s}$, $T_2 \geq 15 \mu\text{s}$, $\tau_{1q} < 1\%$, $\tau_{2q} < 10\%$, admitting 184 paths. Best $F = 0.985$ throughout.

QuBridge displays the circuit alongside its pulse-shape annotation (Fig. 4a).

The effect of pulse-shape on fidelity is modeled as an analytical gate-level proxy rather than through pulse-level Hamiltonian simulation. Shape-dependent error rates, derived from established physical models [4], are applied as Pauli-Lindblad rates in the gate-level noise model, enabling efficient evaluation without solving the Schrödinger equation at the pulse level.

A teleportation circuit uses three gate types, single-qubit rotations (SX/X), two-qubit entangling gates (CZ), and measurement, each with different spectral characteristics. Rather than applying a uniform pulse-shape to all gates, we test whether *per-gate shape assignment* improves fidelity. We compare three uniform-shape configurations (all gates set to Square, Gaussian Square, or DRAG) against a per-gate optimal assignment (SX=DRAG, CZ=Gaussian Square, Meas=Square), selected by matching each gate type to the shape that minimizes its dominant error channel (Fig. 4b).

The per-gate optimal assignment achieves $F=98.49\%$ (SX=DRAG, CZ=Gaussian Sq., Meas=Sq.), outperforming

every uniform shape by at least $+0.36\%$ (Fig. 4b). The improvement arises because different gate types have different dominant error channels (single-qubit rotations favor DRAG, two-qubit gates favor Gaussian Square, measurement is shape-insensitive), and no uniform assignment can match all three simultaneously.

L3’s isolated effect ($+0.87\%$ over All Square) provides a context-fixed reference for the marginal effect observed in §IV-A, where it appears alongside L2’s larger contribution. Per-layer decomposition makes this contextualization observable.

D. Error-Detected Teleportation

We apply the same decomposition framework to error-detected teleportation, testing whether per-layer fidelity decomposition remains valid under encoding. Encoding changes the decision landscape at each layer. At L2, qubit selection shifts from threshold-filtered linear paths (physical) to VF2 subgraph matching (error-detected) with a fixed random seed (seed=42) for deterministic tie-breaking among layouts of equivalent noise score, since the six-qubit $[[2, 1, 1]]$ -encoded circuit requires a connected subgraph that minimizes routing overhead.

Error-detected teleportation is state-dependent (Table III, Fig. 5). For state $|+\rangle$, where Z -error dominates and is undetectable by the $[[2, 1, 1]]$ code, logical fidelity remains below physical across all noise levels and the gap widens from -0.0040 at noise scale 0.5 to -0.0196 at noise scale 2.5. For state $|1\rangle$, where T_1 decay changes the computational-basis parity of the data qubits and is thus flagged by the syndrome, post-selection keeps conditional logical fidelity above physical across the tested range, with the conditional advantage growing from $+0.0049$ at noise scale 0.5 to $+0.0230$ at noise scale 2.5. However, acceptance drops from 96.13% to 82.34%

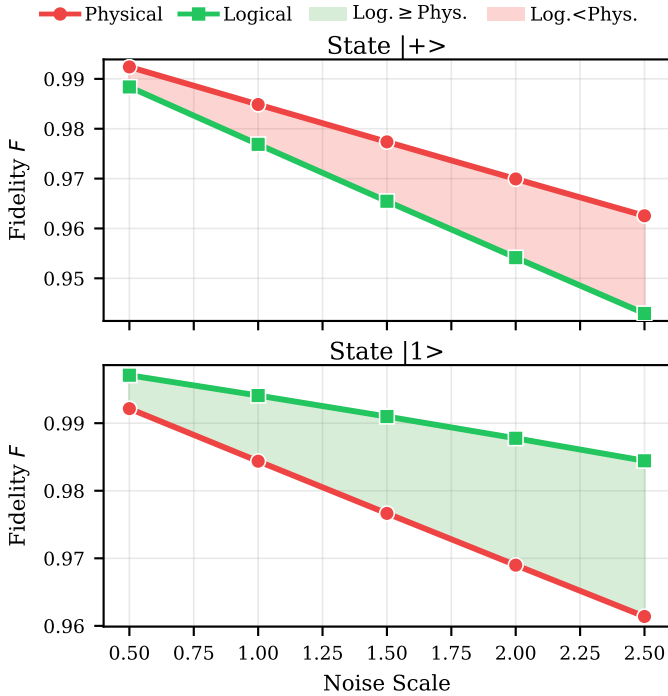


Fig. 5. Teleportation fidelity under increasing noise. For phase-sensitive $|+\rangle$, logical fidelity stays below physical because the $[[2, 1, 1]]$ code cannot detect Z errors. For T_1 -decay-sensitive $|1\rangle$, conditional logical fidelity (after syndrome post-selection on $\{00, 11\}$) exceeds physical across the tested noise range as parity-changing events are removed, with the conditional gap widening as noise grows. Table III reports the corresponding acceptance rates.

TABLE III
TELEPORTATION FIDELITY AND SYNDROME ACCEPTANCE ACROSS NOISE SCALES

Noise	$ +\rangle$ (phase)			$ 1\rangle$ (T_1 decay)		
	Phys. F	Log. F	Accept	Phys. F	Log. F	Accept
0.5	0.9924	0.9884	0.9623	0.9922	0.9971	0.9613
1.0	0.9849	0.9769	0.9263	0.9844	0.9941	0.9244
1.5	0.9774	0.9655	0.8919	0.9767	0.9910	0.8892
2.0	0.9699	0.9541	0.8590	0.9690	0.9878	0.8555
2.5	0.9625	0.9429	0.8275	0.9614	0.9844	0.8234

Noise scale multiplies the calibrated error rates (ns=1.0 matches device calibration). Accept = fraction of shots with syndrome $\in \{00, 11\}$. Logical F is conditional on acceptance; physical acceptance is unity by construction. Sign of ΔF and throughput-adjusted comparison are discussed in Section IV-D.

over the same range, so the throughput-adjusted quantity $\text{Log } F \times \text{Accept}$ favors physical teleportation for state $|1\rangle$ as well, and a fortiori for state $|+\rangle$ where conditional logical fidelity is already below physical. This state-dependent interaction between encoding (L1) and layout optimization (L2) is what the per-layer framework surfaces. Neither decision considered in isolation predicts when encoding pays off.

V. DISCUSSION AND CONCLUSION

We presented QuBridge, a pipeline analysis tool that supports three diagnostic tasks for quantum execution pipelines. Practitioners can identify which layer is responsible for a

fidelity regression, estimate whether an upstream improvement survives downstream transformations, and compare physical and encoded executions under a common decision workflow.

Three findings change how practitioners should interpret fidelity regressions. First, qubit selection acts as a worst-case guarantee rather than a peak-performance lever. Layout choice determines the floor of achievable fidelity, not its ceiling, and this separation is invisible under end-to-end measurement alone. Second, a layer’s measured contribution is context-dependent. The same pulse-shape optimization yields different attributed gains depending on whether upstream layout has been fixed, and per-layer decomposition makes this dependence explicit. Third, error-detection encoding is not uniformly beneficial, and its conditional advantage emerges for input states whose dominant error channel is detectable by the chosen code.

Within the small teleportation circuits evaluated here, L2 and L3 are effectively independent because compact placements within a local qubit cluster keep routing overhead small and layout-independent. For larger circuits whose connectivity exceeds the device’s local topology, SWAP routing becomes unavoidable, so L2’s mapping decision determines circuit depth and thereby the decoherence accumulation that L3’s pulse-shape assignment must mitigate. This tightens the coupling between layers and makes per-layer decomposition more valuable rather than less.

Our evaluation relies on density-matrix simulation with static noise models from IBM Torino calibration data, which provides reproducibility but does not capture crosstalk, spatially correlated errors, or hardware drift. All experiments target IBM Heron architecture, and generalization to other architectures and to larger circuits where L3’s decoherence contribution dominates remains to be validated. The conditional logical fidelity reported in Table III is measured against a noise-aware physical baseline. Both physical and logical layouts were selected by noise score, so any observed advantage represents the residual gain of encoding on top of an already well-chosen layout rather than over an arbitrary placement, and for phase-sensitive states such as $|+\rangle$ no net advantage is observed.

Future work includes quantifying inter-layer coupling at larger circuit scales, extending the framework to variational algorithms, and validating against live hardware.

ACKNOWLEDGMENTS

This work was supported by JST Moonshot R&D Grant Number JPMJMS226C. SN acknowledges support from the JST Moonshot R&D Program Grant No. JPMJMS256G and a JSPS Overseas Research Fellowship. We acknowledge IBM Quantum for the publicly available calibration data and the Qiskit open-source framework. The QuBridge source code, calibration snapshot, and CSV data for all figures and tables are available at <https://github.com/ukinsama/qubridge-qce26> under the MIT license; the artifact reproduces all results without live IBM Quantum hardware access.

REFERENCES

- [1] J. Preskill, “Quantum computing in the NISQ era and beyond,” *Quantum*, vol. 2, p. 79, 2018.
- [2] P. Murali, J. M. Baker, A. Javadi-Abhari, F. T. Chong, and M. Martonosi, “Noise-adaptive compiler mappings for noisy intermediate-scale quantum computers,” in *Proceedings of the 24th International Conference on Architectural Support for Programming Languages and Operating Systems (ASPLOS '19)*. ACM, 2019, pp. 1015–1029.
- [3] S. S. Tannu and M. K. Qureshi, “Not all qubits are created equal: a case for variability-aware policies for NISQ-era quantum computers,” in *Proceedings of the 24th International Conference on Architectural Support for Programming Languages and Operating Systems (ASPLOS '19)*. ACM, 2019, pp. 987–999.
- [4] J. M. Gambetta, F. Motzoi, S. T. Merkel, and F. K. Wilhelm, “Analytic control methods for high-fidelity unitary operations in a weakly nonlinear oscillator,” *Physical Review A*, vol. 83, no. 1, p. 012308, 2011.
- [5] C. Gidney, “Quirk: A drag-and-drop quantum circuit simulator,” <https://algassert.com/quirk>, 2017, accessed: 2026-02-13.
- [6] A. Javadi-Abhari, M. Treinish, K. Krsulich, C. J. Wood, J. Lishman, J. Gacon, S. Martiel, P. D. Nation, L. S. Bishop, A. W. Cross, B. R. Johnson, and J. M. Gambetta, “Quantum computing with Qiskit,” *arXiv preprint arXiv:2405.08810*, 2024, arXiv:2405.08810.
- [7] S. Sivarajah, S. Dilkes, A. Cowtan, W. Simmons, A. Edgington, and R. Duncan, “[t]ket: a retargetable compiler for NISQ devices,” *Quantum Science and Technology*, vol. 6, no. 1, p. 014003, 2021.
- [8] E. Younis, C. Iancu, W. Lavrijsen, M. Davis, E. Smith *et al.*, “Berkeley Quantum Synthesis Toolkit (BQSKit),” <https://github.com/BQSKit/bqskit>, 2021.
- [9] IBM Quantum, “IBM quantum platform,” <https://quantum.ibm.com>, 2016, accessed: 2026-02-13.
- [10] K. Jankiewicz, P. Migdał, and P. Grabarz, “Virtual lab by Quantum Flytrap: Interactive simulation of quantum mechanics,” in *Extended Abstracts of the 2022 CHI Conference on Human Factors in Computing Systems (CHI EA '22)*. ACM, 2022.
- [11] J. Zhao, “Quantum software engineering: Landscapes and horizons,” *arXiv preprint arXiv:2007.07047*, 2020, arXiv:2007.07047.
- [12] M. Piattini, G. Peterssen, R. Pérez-Castillo, J. L. Hevia, M. A. Serrano *et al.*, “The Talavera Manifesto for quantum software engineering and programming,” in *Proceedings of the 1st International Workshop on Quantum Software Engineering and Programming (QANSWER 2020)*, ser. CEUR Workshop Proceedings, vol. 2561, 2020, pp. 1–5.
- [13] J. Wang, Q. Zhang, G. H. Xu, and M. Kim, “QDiff: Differential testing of quantum software stacks,” in *Proceedings of the 36th IEEE/ACM International Conference on Automated Software Engineering (ASE '21)*. IEEE, 2021, pp. 692–704.
- [14] C. H. Bennett, G. Brassard, C. Crépeau, R. Jozsa, A. Peres, and W. K. Wootters, “Teleporting an unknown quantum state via dual classical and Einstein-Podolsky-Rosen channels,” *Physical Review Letters*, vol. 70, no. 13, pp. 1895–1899, 1993.
- [15] L. P. Cordella, P. Foggia, C. Sansone, and M. Vento, “A (sub)graph isomorphism algorithm for matching large graphs,” *IEEE Transactions on Pattern Analysis and Machine Intelligence*, vol. 26, no. 10, pp. 1367–1372, 2004.
- [16] QuTiP Community, “QuTiP virtual lab,” <https://qutip.org/qutip-virtual-lab.html>, accessed: 2026-02-13.
- [17] J. Wang, M. Gao, Q. Wang, T. Zhang, and H. Sun, “Quito: a coverage-guided test generator for quantum programs,” in *Proceedings of the 36th IEEE/ACM International Conference on Automated Software Engineering (ASE '21)*. IEEE, 2021, pp. 1237–1241.
- [18] A. Zeller and R. Hildebrandt, “Simplifying and isolating failure-inducing input,” *IEEE Transactions on Software Engineering*, vol. 28, no. 2, pp. 183–200, 2002.
- [19] J. A. Jones and M. J. Harrold, “Empirical evaluation of the tarantula automatic fault-localization technique,” in *Proceedings of the 20th IEEE/ACM International Conference on Automated Software Engineering (ASE '05)*. ACM, 2005, pp. 273–282.
- [20] E. van den Berg, Z. K. Mineev, A. Kandala, and K. Temme, “Probabilistic error cancellation with sparse Pauli-Lindblad models on noisy quantum processors,” *Nature Physics*, vol. 19, pp. 1116–1121, 2023.
- [21] M. Malekakhlagh, A. Seif, D. Puzzuoli, L. C. G. Góvia, and E. van den Berg, “Efficient Lindblad synthesis for noise model construction,” *npj Quantum Information*, vol. 11, no. 1, p. 191, 2025, arXiv:2502.03462.
- [22] Qiskit Contributors, “Qiskit Aer: High-performance quantum computing simulators with realistic noise models,” <https://github.com/Qiskit/qiskit-aer>, version 0.16.0. Accessed: 2026-02-13.